Available online at www.sciencedirect.com
ScienceDirect
Nuclear Physics B Proceedings Supplement 00 (2014) 1–7
Nuclear Physics B Proceedings Supplement

Performance of the reconstruction, calibration and identification of electrons and photons with the ATLAS detector, and their impact on the ATLAS physics results

J-B. Blanchard[1], on behalf on the ATLAS Collaboration

IRFU, CEA-Saclay, Batiment 141, F-91191 Gif-sur-Yvette Cedex

Abstract

The performance of the reconstruction, calibration and identification of electrons and photons with the ATLAS detector at the LHC is a key component to realise the ATLAS full physics potential, both in the searches for new physics and in precision measurements. For instance, they all played a critical role in the discovery of a Higgs boson, announced by the ATLAS Collaboration in 2012, and in the measurement of its properties. This proceedings presents a description of the algorithms used for the reconstruction and identification of electrons and photons with the ATLAS detector, as well as results from the measurements of their efficiencies in pp collisions. The electron and photon energy calibration procedure is discussed, as well as its impact on the precise measurement of the Higgs boson mass.

Keywords: electron, photon, calibration, identification, efficiency, Higgs

1. Introduction

The Brout-Englert-Higgs particle discovery has been claimed in July 2012 both by the ATLAS [1] and the CMS [2] collaborations through bosonic decays: in two photons ($\gamma\gamma$), in two Z bosons with a 4 leptons final state (ZZ) and in two W bosons with two leptons and two neutrinos in the final state (WW). In the latest Higgs mass measurement released by ATLAS [3], that relies mostly on the two former channels, the electron and photon calibration uncertainty, which was one of the largest systematic uncertainties, has been nicely reduced. Improving the reconstruction and identification efficiency measurements helps also reducing the statistical uncertainty by getting the largest signal sample while rejecting as much backgrounds as possible. These effects show the necessity to have photons and electrons reconstructed as precisely as possible.

In this proceedings, the electron reconstruction strategy is briefly introduced along with its efficiency measurement. The new electrons and photons calibration procedure is then discussed through several of its main steps, showing the improvements reached with respect to the previous scheme used. Finally both electron and photon identification are discussed and their efficiency measurements are presented. All these studies are done using data collected with $\sqrt{s}$ =8 TeV taken in 2012 at the LHC. Throughout this proceedings, the Higgs bosonic decays (to $\gamma\gamma$ and ZZ) are used as physics case to illustrate the impact of all these various performances.

2. Reconstruction of electrons

The electron reconstruction [4] in the central region of the ATLAS detector [5] ($|\eta| < 2.47$) starts from energy deposits (cluster) in the electromagnetic (EM) calorimeter which are then associated to reconstructed tracks of charged particles in the inner detector (ID).

2.1. Reconstruction principle

The first step is to reconstruct the clusters in the EM calorimeter. For electrons, this is done with an efficiency of 95% for E_T=7 GeV that reaches 99%

[1]jean-baptiste.blanchard@cern.ch

for E_T=15 GeV and 99.9% for E_T=45 GeV. For every cluster passing loose shower shape requirement, a region-of-interest is defined, with a cone-size of ΔR=0.4 around the cluster barycenter, in which the track reconstruction is performed.

This "stage" is done in a two-step procedure that has been improved for the 2012 data taking period in order to account for possible bremsstrahlung. It consists in a pattern recognition with either a pion hypothesis or a Kalman filter-smoother formalism [6] (which allows at most 30% energy loss at each material surface) followed by a track fit using the corresponding previous hypothesis. At this point, the track-candidates parameters are precisely re-estimated using an optimised electron track fitter, the Gaussian Sum Filter (GSF) [7] algorithm. It yields a better estimate of the track parameters, especially in the transverse plane, by accounting for the non-linear bremsstrahlung effects. The tracks are then used to perform the final track-cluster matching.

Each of these electron clusters is then rebuilt in all four layers sequentially, starting from the middle layer, using 3×7 (5×5) cells in $\eta \times \phi$ in the barrel (endcaps) of the EM calorimeter. The cluster position is adjusted in each layer to take into account the distribution of the deposited energy. These lateral cluster sizes have been optimised to take into account the different overall energy distributions in the barrel and endcap accordion calorimeters specifically for electrons.

2.2. Efficiency determination

Reconstruction efficiencies have been measured with the tag-and-probe technique using electrons from Z boson decays. This allows getting (η_ℓ,p_T^ℓ) dependent measurement with a lower bound on electron E_T of 15 GeV. Below this threshold, efficiencies are taken from simulation with a 2% (5%) uncertainty in the barrel (endcaps). Between 15 and 25 GeV, efficiencies are varying from 95 to 99% with an uncertainty of 0.5 to 2% and they are reaching 98-99% with 0.5% uncertainty when E_T>25 GeV.

Figure 1 shows the evolution of the reconstruction efficiencies as a function of E_T (integrated over η_ℓ), using 2011 and 2012 data and simulations. There is an overall improvement of 5% with the new track reconstruction used in 2012 that can reach up to 7% for the lower E_T region. This is an important improvement for analyses like the Higgs decaying into ZZ as the lepton p_T spectrum is expected to extend till small values with a light Higgs boson.

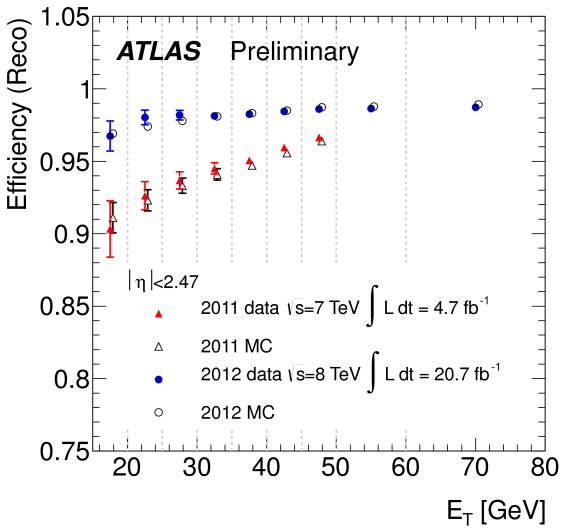

Figure 1: Evolution of reconstruction efficiencies as a function of E_T (integrated over η_ℓ), using 2011 (red) and 2012 (blue) data and simulation.

3. Calibration of electrons and photons

In this section, the new calibration procedure [8] is introduced and several of its key aspects are detailled. Various cross-checks are also presented along with the highlights of the impact of this new calibration scheme on the Higgs boson mass measurement analysis.

3.1. Calibration overview

The new calibration has been derived using the complete run I data. It can be decomposed into several steps (some of which are applied only to data, the rest both to data and simulation), starting with the measurement of the energy deposit in the EM calorimeter. To a large extent, this new procedure is taking advantage of the longitudinal segmentation of the EM calorimeter. There is indeed three longitudinal layers (named strip, middle and back layers) with different η,ϕ granularity and a presampler (PS) for $|\eta_\ell|$ <1.8. This is shown in Figure 2, where a schematic drawing of the interaction of particles is made with the EM calorimeter in two different region of pseudorapidity.

The EM cluster properties and additional information from the ATLAS ID are linked to the true electron and photon energy in simulated samples using multivariate analysis (MVA). The optimisation of this MVA calibration is performed separately for electrons and photons, spltting photons into converted and unconverted ones. A pre-requisite of this MC-based calibration is that the detector description and the particle-to-matter interaction

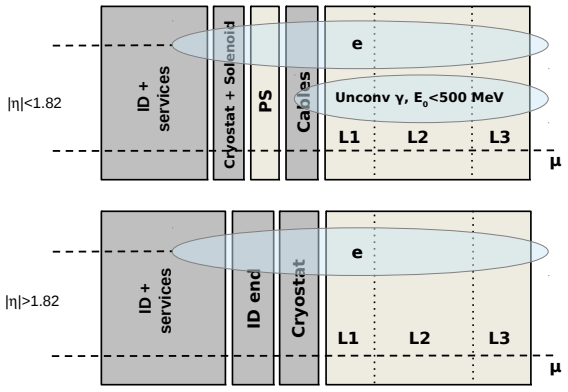

Figure 2: Schematic overview of the longitudinal shower profile for electrons, unconverted photons and muons in the EM calorimeter below (top) and beyond (bottom) $|\eta_\ell|$=1.82.

are accurately described in the simulation. The material distribution in data are measured using the ratio (L1/L2) of energy in the first (L1) over second (L2) layer of the longitudinally segmented EM calorimeter as it is discussed in § 3.3.

Before the MVA calibration is applied to the cluster energies reconstructed from data, a set of corrections are implemented to account for response details not included in the simulation in specific detector regions, *e.g.*, non optimal high-voltage (HV) regions, transitions between barrel calorimeter modules and so on.

Since the EM calorimeter is longitudinally segmented, the scales of the different longitudinal layers have to be equalised in data with respect to simulation. The procedure to measure the EM calorimeter layer scales has been reviewed and is discussed in § 3.2.

The electron and photon absolute responses are finally matched between data and simulation using a large sample of Z bosons decaying to two electrons. A new set of scale-corrections have been extracted for data along with resolution corrections to be applied to simulation because not all experimental effects are accounted for. This step is detailled in § 3.4.

3.2. Relative calibration of strip and middle layer

This section presents the intercalibration of the first and second accordion layers done by studying the ratio of energy in the first over second layer, E_1/E_2, called hereafter $E_{1/2}$, using muons from Z boson decays. Discussion of the PS scale measurement can be found in Ref. [8]. No dedicated intercalibration of the back layer has been carried out.

The muon energy deposits in the calorimeter are insensitive to the amount of passive material upstream of the EM calorimeter and constitute a direct probe of the energy response. The measured muon energy is typically 60 MeV in the strips and about 210 MeV in the middle layer, with a signal to noise ratio of about 3. Muon energy deposits are very localised, most of the energy being deposited in one or two cells.

The observed muon energy distribution in each layer is given by the convolution of a Landau distribution describing the energy deposit, and a Gaussian distribution corresponding to the electronic noise. The most probable value (MPV) of the deposited energy is extracted using either an analytic fit following the above model, or from a truncated mean method. The intercalibration result, defined as $\alpha_{1/2} = \langle E_{1/2}\rangle^{\rm data}/\langle E_{1/2}\rangle^{\rm MC}$ is given by the average of the two MPV extraction methods, the difference being used to define its systematic uncertainty. The resulting values are presented in Figure 3 as a function of the lepton pseudorapidity and shows a bias of up to 5% which is removed by applying an $|\eta|$-dependent correction to the energy measured in the middle layer in data ($E_2^{\rm corr} = E_2 \times \alpha_{1/2}$).

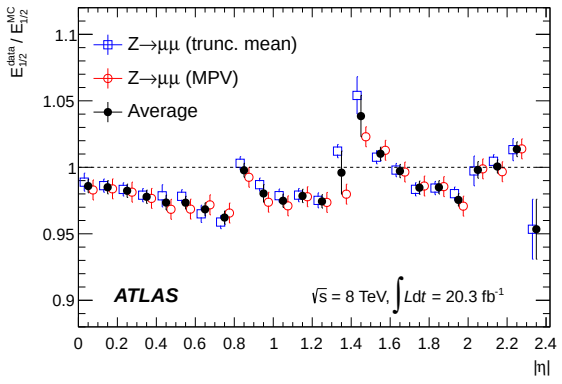

Figure 3: The ratio $\langle E_{1/2}\rangle^{\rm data}/\langle E_{1/2}\rangle^{\rm MC}$, as obtained from both fit and truncated mean methods. The error bars represent the total uncertainty specific to the $Z \to \mu\mu$ analysis.

Different sources of uncertainties have been considered (geometry of read-out and electric field, cross-talk within one layer and from one layer to another, and others) giving rise to an impact on the relative calibration $\alpha_{1/2}$ going from 1% to 1.5% in the barrel and of 1.5% in the endcap. These uncertainties are also propagated to uncertainties on the modelling of $E_{1/2}$ for electrons and photons, as this variable is used in § 3.3 for the passive-material determination.

3.3. Improving the detector material simulation

After L1/L2 calibration corrections extracted using muons, the electrons and photons $E_{1/2}$ distributions can be used to quantify the amount of detector material upstream of the active calorimeter, since higher values of $E_{1/2}$ in data indicating earlier shower development, and hence a local excess of material in comparison with the simulation.

This missing passive material can be regrouped in ID material, cryostat material located between the maximal conversion radius and the PS, and calorimeter material located between the PS and L1. Electrons are sensitive to all detector material crossed along their trajectory whereas unconverted photons, chosen with a veto on the PS activity (E_0) to minimise the probability that a conversion happened in front of the PS, are sensitive to passive material between the PS and L1. The corresponding shower developments are sketched in Figure 2 and the sensitivity of $E_{1/2}$ for these probes of detector material is evaluated using simulated samples with modified geometries.

For each material variations and in a given $|\eta|$ region, the amount of additional material X is normalised to the relative shift induced in $E_{1/2}$ for electrons or photons respectively, obtaining a sensitivity factor $\frac{\partial X/X_0}{\partial_{\rm rel} E_{1/2}}$. This factor is scaled by the observed relative difference $\Delta E^{\rm data}_{1/2}$ of $E_{1/2}$ between data and simulation after calibration corrections yielding an estimate of the passive-material offset with respect to the nominal simulation.

Two categories of detector material are probed for $|\eta| < 1.82$: the integral between the interaction point and the PS, *i.e.* the sum of ID and cryostat material; and calorimeter material between the PS and L1. The former is obtained by comparing $E_{1/2}$ in the electron and unconverted photon data samples while the latter is obtained by comparing $E_{1/2}$ for unconverted photons between data and simulation. For $|\eta| > 1.82$, only the integral up to L1 is measured, by comparing $E_{1/2}$ for electrons between data and simulation. The results of this procedure is shown for the previous detector description in Figure 4.

After calibration corrections, the unconverted photon $E_{1/2}$ distributions show no significant bias, translating into calorimeter material discrepancies of at most $0.03X_0$, with an accuracy of about $0.03X_0$. The material difference integrated up to L1 shows moderate features in the barrel whereas strong excesses, up to $0.6{-}0.7X_0$, can be seen in the endcap, in the region $1.65 < |\eta| < 1.75$, and around $|\eta| = 1.9$ because of an incomplete description of silicon microstrip cooling pipes. The material bias integrated up to the PS is obtained after subtracting, from the above, material contributions located after the PS. The features observed within the PS acceptance are very similar to previously described ones, which indicates that the material biases are located upstream of the PS. For both integrated estimates, the measurement accuracy ranges from about $0.04X_0$ to $0.06X_0$.

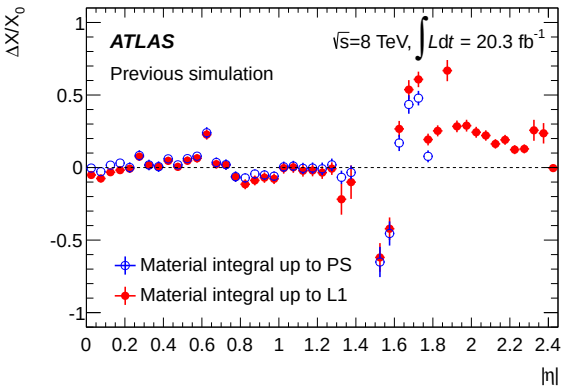

Figure 4: Difference between the material estimate from data and the previous simulation, integrated up to L1 and up to the PS.

Given the absence of significant biases in the calorimeter material, the data suggest implementing material simulation modifications upstream of the PS. Most of the discrepancies correspond to areas with a large amount of material from services between the ID active area and the calorimeter cryostat. The corrections were implemented in an effective way, adding material in these most discrepant areas and in amounts corresponding to the measurement, leading to an improved simulation. The complete set of analyses previously detailled has been redone, using this new simulation shown in Figure 5.

The new simulation behaves as expected in most of the acceptance: the overall discrepancy in the endcap has disappeared, as well as the strong peak around $|\eta| = 1.9$. The deficit within $1.5 < |\eta| < 1.6$ remains, as it has not been addressed. In the barrel, the excess at $|\eta| = 0.6$ has been halved. Studies using K^0_S decays, secondary hadronic interactions and photon conversions were also performed [9, 10], with no indication of ID material mis-modelling larger than 5%. The $E_{1/2}$ analysis constrain the later material (invisible to the tracker) to 2-5% X_0.

The MC-based energy calibration is trained using the new detector description. The resulting MC calibration forms the basis of the absolute scale determination presented in the next section.

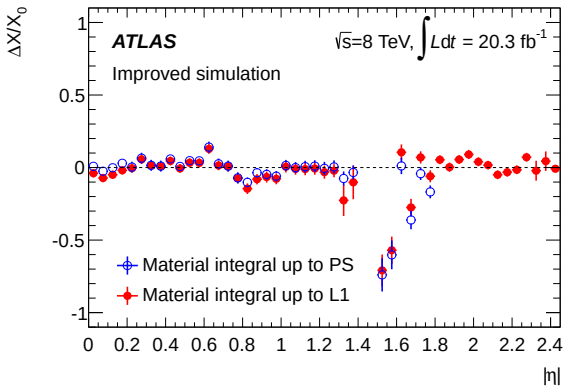

Figure 5: Difference between the material estimate from data and the new simulation, integrated up to L1 and up to the PS.

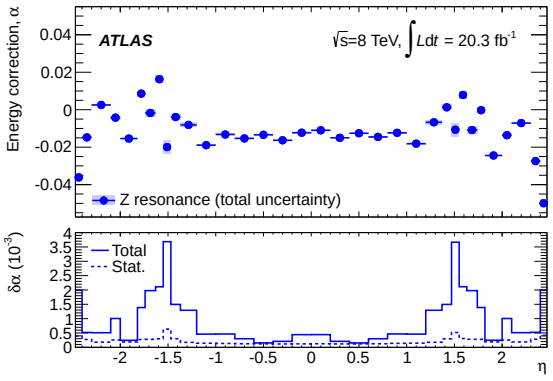

Figure 6: Top: energy scale corrections α derived from $Z \to ee$ events using the template method. The corrections are defined after uniformity and layer calibration corrections. The error bands include statistical and systematic uncertainties. Bottom: statistical and total energy scale uncertainties.

3.4. Energy scale and resolution from Z boson

The energy mis-calibration is defined as the difference in response between data and simulation, and is formalised as $E^{\text{data}} = E^{\text{MC}}(1 + \alpha)$, where E^{data} and E^{MC} are the electron energy in data and simulation, and α represents the departure from optimal calibration. Electron resolution corrections are derived under the assumption that the resolution curve is well modelled by the simulation up to a Gaussian constant term. Both energy scales and resolution corrections are extracted as a function of the electron pseudorapidity, using reconstructed Z boson decays, adjusting the invariant mass with the template and fit methods.

The energy scale values extracted from this measurement are shown in Figure 6 and are accurate to $0.3{\times}10^{-3}$ for $|\eta| < 1.37$, 2×10^{-3} for $1.37 < |\eta| < 1.82$ and 0.5×10^{-3} for $|\eta| > 1.82$. These uncertainties include method difference, selection and fit range variations, momentum lost by bremsstrahlung. The resolution corrections are found to be about 0.8% on average in the barrel, and about 1% in the endcap, and are determined to be accurate on average to 0.3% and 0.5%, respectively. At given $|\eta|$, their values are found to be statistically compatible for $\eta > 0$ and $\eta < 0$ and are averaged.

3.5. Cross-checks of the new calibration scheme

Using this new calibration scheme (including the previously discussed energy scale and resolution corrections), several cross-checks have been performed to validate the procedure. Among these tests, photon energy scales have been extracted using radiative Z decays. The results are found to be compatible within uncertainties (including specific photon uncertainties) with results shown in Figure 6. J/ψ decays to two electrons have also been used to extract energy scales as a function the lepton E_T, whose measurements are found to be compatible with results from Z boson within the uncertainties as shown in Figure 7.

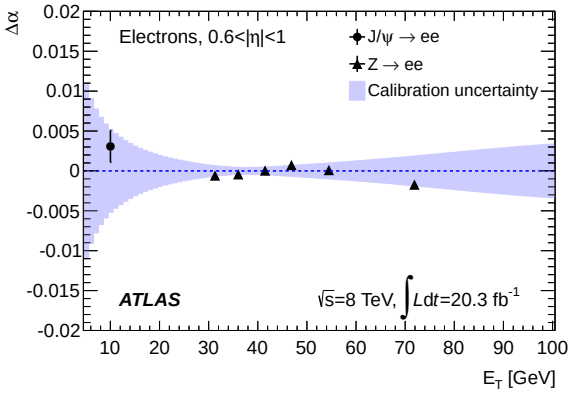

Figure 7: Energy scale obtained after full calibration procedure from the J/ψ and the Z analyses, as function of E_T, for $0.6 < |\eta| < 1.0$. The band represents the calibration systematic uncertainty.

3.6. Stability and impact on Higgs boson mass

The stability of the calorimeter energy response obtained after the corrections of the new calibration procedure (mentioned in § 3.1 but not discussed precisely here) have been measured as a function of the mean number of interactions per bunch crossing (μ), and as a function of time. These measurements, performed with Z boson decays using two methods, show stability at the level of 0.05% as a function of the mean number of

interactions per bunch crossing, as shown in Figure 8. Same accuracy is reached when looking as a function of time.

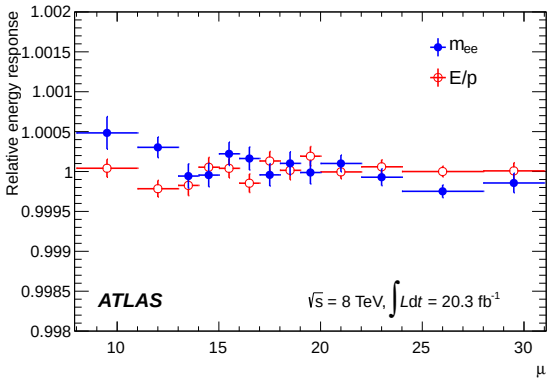

Figure 8: Energy response as a function of the mean number of interactions per bunch crossing (μ), normalised to its average, measured with two methods.

With respect to the previous calibration scheme, the new procedure shows a large improvement of the understanding of our detector description, leading to a recalibration of the EM calorimeter layers and an estimation of absolute energy scales and resolution with drastically reduced uncertainties, both for photons and electrons. This new procedure is leading to a resolution improvement of the Higgs boson mass (decaying to two photons) by 10% and a reduction of the total mass systematic uncertainty from this and other improvements by a factor 2.5 [3] with respect to the previous measurement [11].

4. Electrons and photons identification

The electrons [4] and photons [12] identification level defines the object-quality, based on a various set of discriminating variables describing track parameters and calorimeter energy deposits. The corresponding efficiencies have been estimated, with respect to reconstruction level, using tag-and-probe technique, and are introduced in the following sections.

4.1. Electrons identification

In 2011, the identification menu was defined using a cut-based (CB) selection, creating four operating points, called *loose*, *multilepton*, *medium* and *tight*, which are ordered by decreasing efficiency, in favour of an increasing background rejection. These operating points use track parameters information, calorimeter energy deposits and the track-cluster matching description.

Another identification menu has also been defined using multivariate analysis, in order to get a larger background rejection keeping the same efficiency level. The discriminating variables used in this analysis are the same as the ones used for the CB definition adding few other variables sensitive to bremsstrahlung effects. The likelihood (LH) selection provides three operating points: LOOSE, MEDIUM and VERY TIGHT, whose efficiencies correspond respectively to the CB *multilepton*, *medium* and *tight* selections.

The efficiencies for all the menu and operating points are evaluated with the tag-and-probe method using Z decay to two electrons, Z decay to two electrons and a photon and J/ψ decay to two electrons. These different sources allowed measurements of efficiency for electrons respectively with E_T>15 GeV, 10<E_T<15 GeV and 7<E_T<20 GeV. This helps to reduce the uncertainty for the low-E_T electrons. These measurements are done integrated and differentially as functions of the lepton pseudorapidity and E_T.

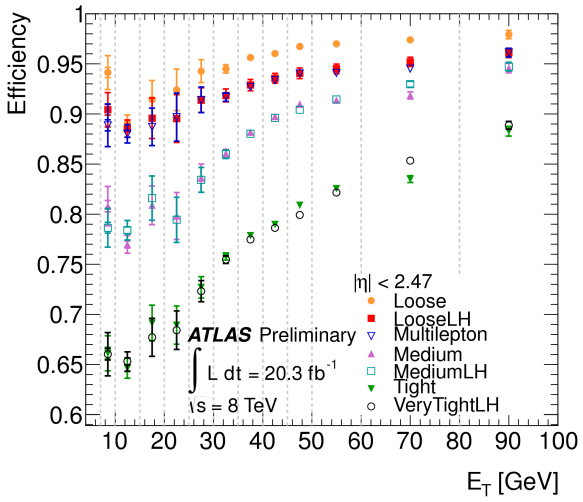

Figure 9: Measured identification efficiency for the various cut-based and likelihood selections as a function of E_T.

The efficiencies as a function of E_T, integrated over pseudorapidity, are displayed in Figure 9. The uncertainties are close to 1-2% (6%) for E_T> (<) 25 GeV. The dependence on both pseudorapidity and E_T are understood as well as the difference between one operating point and another. The background rejection factor is improved by ~40% when using LH menu, and the ratios of efficiencies from data to MC are close to 1.

4.2. Photons identification

As for the electrons, the photons identification have been estimated splitting both the MC and data sample into converted and unconverted photons. A tag-and-probe method has been used with radiative Z decay providing efficiency for photon probes with $10<E_T<80$ GeV. Two other methods were used, one relying on the shower shape extrapolation from electrons coming out from Z decay, covering photons with $30<E_T<100$ GeV and another one using a so-called "matrix method", using purity and isolation information, that covers a wide range of photons with $E_T>20$ GeV.

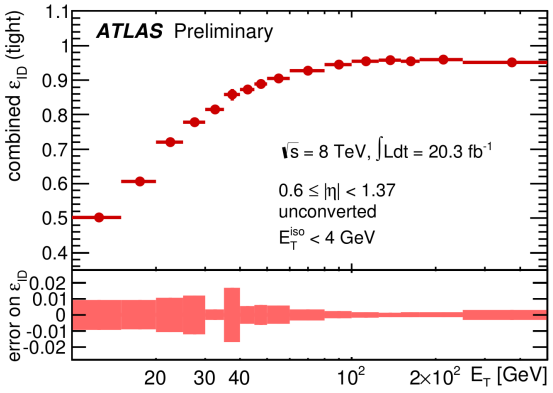

Figure 10: Measured identification efficiency for the unconverted photons with a pseudorapidity between 0.6 and 1.37, as a function of E_T.

The resulting efficiencies, shown for example in Figure 10 for unconverted photons with a pseudorapidity between 0.6 and 1.37, have uncertainty around 1% (1.5%) for unconverted (converted) photons with $E_T<30$ GeV. For photons with $50<E_T<200$ GeV, these uncertainties become close to 0.4-0.5%.

5. Conclusion

This proceedings presents the reconstruction and identification efficiencies of electrons and photons, using J/ψ and Z decays (including those with radiative photons) and inclusive photon samples. Important improvements have been made, mostly based on a new track algorithm and track-cluster matching, enhancing the reconstruction efficiency by ~7% at low E_T, as well as a likelihood identification discriminant, improving the background rejection by 30 to 50% for a fixed efficiency. This is helping getting a high selection efficiency of Higgs decaying to ZZ while keeping the background rejection as high as possible.

A new calibration scheme using a new detector description correcting for passive material and a recalibration of the different EM calorimeter layers has also been presented. The calorimeter energy measurement has now reached a stability over time and pile-up at ~0.05%. The absolute energy scale and resolution have been extracted using Z boson decays, reaching an accuracy on the scale of ~0.04%. This new procedure is leading to a resolution improvement of the Higgs boson mass (decaying to two photons) by 10% and a reduction of the total mass systematic uncertainty from this and other improvements by a factor 2.5 [3] with respect to the previous measurement [11].

References

[1] ATLAS Collaboration, Observation of a new particle in the search for the Standard Model Higgs boson with the ATLAS detector at the LHC, Phys. Lett. B716 (2012) 1–29.
[2] CMS Collaboration, Observation of a new boson at a mass of 125 GeV with the CMS experiment at the LHC, Phys. Lett. B716 (2012) 30–61.
[3] ATLAS Collaboration, Measurement of the Higgs boson mass from the $H \to \gamma\gamma$ and $H \to ZZ^* \to 4\ell$ channels with the ATLAS detector using 25 fb^{-1} of pp collision data, Phys. Rev. D90 (2014) 052004.
[4] ATLAS Collaboration, Electron efficiency measurements with the atlas detector using the 2012 lhc proton-proton collision data, ATLAS-CONF-2014-032, https://cds.cern.ch/record/1706245.
[5] ATLAS Collaboration, The ATLAS Experiment at the CERN Large Hadron Collider, JINST 3 (2008) S08003.
[6] R. Frühwirth, Application of Kalman filtering to track and vertex fitting, Nucl. Instrum. Meth. A262 (1987) 444–450.
[7] ATLAS Collaboration, Improved electron reconstruction in ATLAS using the Gaussian Sum Filter-based model for bremsstrahlung, ATLAS-CONF-2012-047, https://cds.cern.ch/record/1449796.
[8] ATLAS Collaboration, Electron and photon energy calibration with the ATLAS detector using LHC Run 1 data. arXiv:1407.5063.
[9] ATLAS Collaboration, Study of the Material Budget in the ATLAS Inner Detector with K0S decays in collision data at $\sqrt{s}$ = 900 GeV, ATLAS-CONF-2010-019, https://cds.cern.ch/record/1277651.
[10] ATLAS Collaboration, Charged-particle multiplicities in pp interactions measured with the ATLAS detector at the LHC, New J. Phys. 13 (2011) 053033.
[11] ATLAS Collaboration, Measurements of Higgs boson production and couplings in diboson final states with the ATLAS detector at the LHC, Phys. Lett. B726 (2013) 88–119.
[12] ATLAS Collaboration, Measurements of the photon identification efficiency with the ATLAS detector using 4.9 fb[1] of pp collision data collected in 2011, ATLAS-CONF-2012-123, https://cds.cern.ch/record/1473426, updated plots: https://atlas.web.cern.ch/Atlas/GROUPS/PHYSICS/-EGAMMA/PublicPlots/20140611/ATL-COM-PHYS-2014-542/index.html.